THE EFFECT OF CANDU FUEL BUNDLES ENDPLATE/ENDCAP WELD MORPHOLOGY ON COMPUTED STRESS INTENSITY FACTORS AT THE WELDS

NWMO TR-2011-03 **April 2011**

Bogdan S. Wasiluk

Kinectrics, Inc.

nwmo

NUCLEAR WASTE MANAGEMENT ORGANIZATION

SOCIÉTÉ DE GESTION DES DÉCHETS NUCLÉAIRES

Nuclear Waste Management Organization
22 St. Clair Avenue East, 6th Floor
Toronto, Ontario
M4T 2S3
Canada

Tel: 416-934-9814
Web: www.nwmo.ca

THE EFFECT OF CANDU FUEL BUNDLES ENDPLATE/ENDCAP WELD MORPHOLOGY ON COMPUTED STRESS INTENSITY FACTORS AT THE WELDS

NWMO TR-2011-03

April 2011

Bogdan S. Wasiluk
Kinectrics, Inc.

ABSTRACT

Title: **The Effect of CANDU Fuel Bundles Endplate/Endcap Weld Morphology on Computed Stress Intensity Factors at the Welds**
Report No.: **NWMO TR-2011-03**
Author(s): Bogdan S. Wasiluk
Company: Kinectrics, Inc.
Date: April 2011

Abstract
Delayed hydride cracking has been identified as a potential degradation mechanism of the endplate-to-endcap assembly welds in CANDU fuel bundles during long-term dry storage. Consequently, in order to assess whether DHC is a concern, the stress intensity factor for DHC initiation of Zircaloy endplate-to-endcap assembly welds needs to be established. This parameter will be used in deterministic and probabilistic assessments of the structural integrity of the fuel bundles.

This report discusses the effects of fuel element and endplate geometry, weld morphology and endplate-to-endcap weld on computed stress intensity factors. The stress intensity factors were computed from the *J*-integral or *I*-integral using the finite element method. The stress intensity factors for mode I, II and III loading were also determined in order to investigate the deformation of the crack front.

Results from this investigation led to the following conclusions:

- The calculated stress intensity factors show a strong dependence on circumferential extension of an endplate-to-endcap weld discontinuity up to a ninety degree from the top of the weld. Beyond the ninety degrees, the susceptibility is less pronounced.

- The shape of the endplate-to-endcap weld discontinuity, round versus elliptical, was found to play a minor role in the representative depth of the endplate-to-endcap weld discontinuity.

- Deformation of the endplate significantly changes distribution of stresses at the endplate-to-endcap weld discontinuity.

- The maximum value of stress intensity factor could be re-located from the vertical plane to a plane at forty five degree from the vertical for a GE-1 type fuel element.

- The position of the endcap regarding to the endplate strongly affect stress intensity factors. The maximum value of the stress intensity factor could be moved from the plane at forty five degree to the vertical plane because of it.

- Uncertainties in characterization of the endplate-to-endcap weld discontinuity leads to considerable error in the calculated stress intensity factor.

- An endplate-to-endcap weld discontinuity could be under complex combined modes I, II and III crack loading during both experiment and during fuel bundle storage.

TABLE OF CONTENTS

LIST OF TABLES

Page

LIST OF FIGURES

Page

Abbreviations and Acronyms

DHC - Delayed Hydride Cracking
GE - General Electric
GE-1 - 28-Elements Fuel Bundle of General Electric Design
GE-2 - 37-Elements Fuel Bundle of General Electric Design

Nomenclature

a - crack length
E - Young's modulus
I - I-integral
J - J-integral
J^{CD} - J-integral of surface crack with constant depth
J^{EL} - J-integral of surface crack with elliptical crack shape
K - stress intensity factor
K_I - mode I stress intensity factor
K_I^{CD} - mode I stress intensity factor of surface crack with constant depth
K_I^{EL} - mode I stress intensity factor of surface crack with elliptical crack shape
n - strain hardening exponent
u_i - displacements
r ,θ - components of polar co-ordinate system
T - T-stress
σ_{ii} - stresses
v - Poisson's ratio

Units Table

Dimensions- mm
Force - N
Stress - MPa

1. INTRODUCTION

Delayed hydride cracking (DHC) has been demonstrated as a possible degradation mechanism of the endplate-to-endcap assembly welds in CANDU fuel bundles (Shek and Wasiluk, 2009). The stress intensity factor for DHC initiation, K_{IH}, of Zircaloy endplate-to-endcap assembly welds due to the weld discontinuity needs to be established. This parameter will be used for deterministic and probabilistic assessments of the structural integrity of CANDU fuel bundles in long term dry storage.

The morphology of endplate-to-endcap assembly welds is different depending on the fuel bundle design. This study is focused on analysis of the fuel bundle design by General Electric (GE) for 28 (GE-1) and 37 elements (GE-2) CANDU fuel bundles. The fuel elements of these fuel bundles have different geometry. For fuel elements of GE-1 design the position of the endcap-weld is moved from the center of the endplate. This introduces different loading conditions.

This report discusses the effects of fuel element and endplate geometry and endplate-to-endcap weld discontinuity on the computed stress intensity factors. The stress intensity factors were computed from the *J*-integral and *I*-integral using the finite element method. Three dimensional models were developed using 20-node elements with reduced integration order. Stress intensity factors for mode I, II and III loading were also computed to investigate deformation at the crack front during fracturing.

This report is organized as follows:

- Section 2 presents the fundamentals of fracturing and calculation methodologies.
- Section 3 analyzes the effect of endcap-endplate weld discontinuity geometry on stress intensity factors.
- Section 4 discusses stress intensity factors of non-irradiated 37 and 28 element General Electric CANDU fuel bundles.
- Section 5 summarizes the results and provides conclusions.

2. FRACTURE MECHANICS CRACK DRIVING FORCE

2.1 STRESS INTENSITY FACTOR

The stress field at the crack tip in an elastic solid as derived by Williams (1957) has the following form:

$$\sigma_{ij}(r,\theta) = A_m^{(1)} r^{-1/2} f_{ij}^{(1)}(\theta) + A_m^{(2)} f_{ij}^{(2)}(\theta) + A_m^{(3)} r^{1/2} f_{ij}^{(3)}(\theta) + \ldots \quad (1)$$

where *r* and *θ* are components of the polar co-ordinate system centered at the crack tip (see Figure 1) and $i, j = 1,2,3$. The intensity of the elastic stress field is characterized by $A_m^{(1)}$ which is the stress intensity factor K_i.

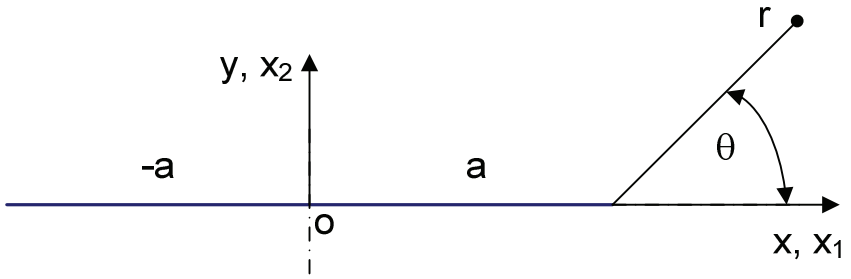

Figure 1: A Crack in Polar and Cartesian Coordinate Systems

In Equation (1), amplitude $A_m^{(2)}$ has the dimensions of stress, and it is named the *T*-stress. Considering *T*-stress in Equation (1) for opening mode of crack loading, one obtains for pure mode I:

$$\begin{Bmatrix} \sigma_{xx} \\ \sigma_{yy} \\ \tau_{xy} \end{Bmatrix} = \frac{K_I}{\sqrt{2\pi r}} \cos\frac{\theta}{2} \begin{Bmatrix} 1 - \sin\frac{\theta}{2}\sin\frac{3\theta}{2} \\ 1 + \sin\frac{\theta}{2}\sin\frac{3\theta}{2} \\ \sin\frac{\theta}{2}\cos\frac{3\theta}{2} \end{Bmatrix} + \begin{Bmatrix} T \\ 0 \\ 0 \end{Bmatrix} + O\left(r^{1/2}\right) \quad (2)$$

where K_I is stress intensity factor of mode I crack loading.

A crack could be loaded in single or combined modes. Figure 2 shows three principal crack loading modes (a) opening - mode I, (b) in-plane shear – mode II and (c) anti-plane shear – mode III.

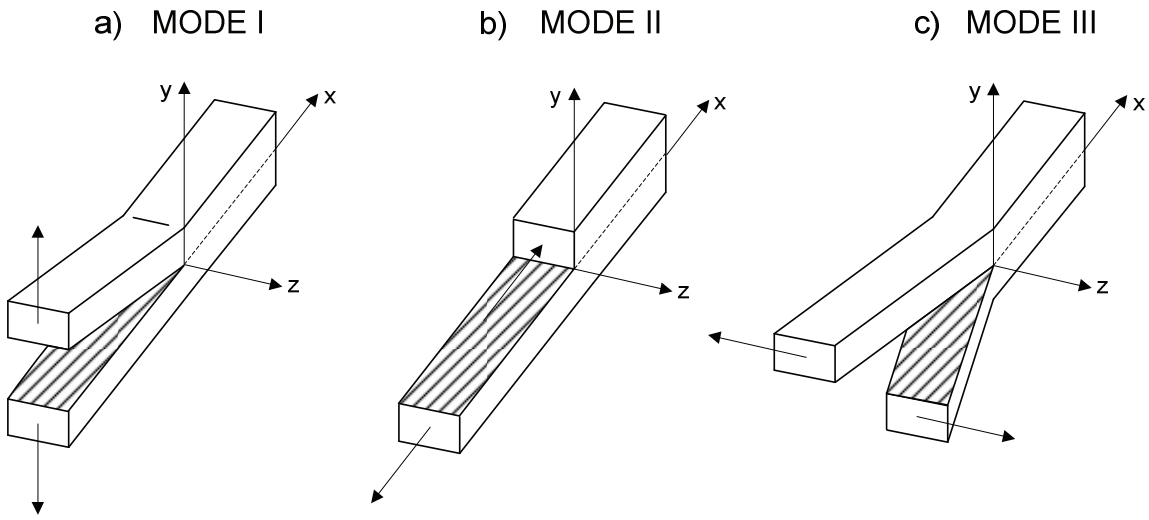

Figure 2: Crack Loading Modes: (a) Opening, (b) In-Plane Shear and (c) Anti-Plane Shear

The stress field ahead of the crack tip under mode II loading is

$$\begin{Bmatrix} \sigma_{xx} \\ \sigma_{yy} \\ \tau_{xy} \end{Bmatrix} = \frac{K_{II}}{\sqrt{2\pi r}} \begin{Bmatrix} -\sin\frac{\theta}{2}\left(2+\cos\frac{\theta}{2}\cos\frac{3\theta}{2}\right) \\ \sin\frac{\theta}{2}\cos\frac{\theta}{2}\cos\frac{3\theta}{2} \\ \cos\frac{\theta}{2}\left(1-\sin\frac{\theta}{2}\sin\frac{3\theta}{2}\right) \end{Bmatrix} \quad (3)$$

where K_{II} is the stress intensity factor of mode II crack loading. Under mode III crack loading, the stress field ahead of the crack tip is:

$$\begin{Bmatrix} \tau_{xz} \\ \tau_{yz} \end{Bmatrix} = -\frac{K_{III}}{\sqrt{2\pi r}} \begin{Bmatrix} \sin\frac{\theta}{2} \\ \cos\frac{\theta}{2} \end{Bmatrix} \quad (4)$$

where K_{III} is the stress intensity factor of mode III crack loading.

Under combined I+II+III crack loading, the linear elastic stress state is obtained by stress superposition.

2.2 J-INTEGRAL

The nonlinear elastic stress field at the crack tip under proportional loading is given by Hutchinson (1968) and Rice and Rosengren (1968) as:

$$\frac{\sigma_{ij}}{\sigma_y} = \left(\frac{J}{\alpha \varepsilon_y \sigma_y I_n r} \right)^{1/(n+1)} \tilde{\sigma}_{ij}(\theta, n) \quad (5)$$

where I_n is an integration constant depending only on the strain hardening exponent n, ε_y is yield strain, σ_y is yield strength and $\tilde{\sigma}_{ij}$ is a dimensionless function. Equation (5) was derived by assuming the non-linear material properties are characterized by the Ramberg-Osgood equation (Gellerud *et al*, 2007 and 2009). Equation (5), similarly to Equation (2), shows a $1/\sqrt{r}$ stress singularity.

The *J*-integral is energy release rate or an amplitude or intensity of nonlinear stress field and usually defined as per Hutchinson (1968) and Rice and Rosengren (1968) as:

$$J_i = \int_{\Gamma} \left(w dx_2 - \sigma_{ij} n_j \frac{\partial u_i}{\partial x_1} ds \right) \quad (6)$$

where Γ is the integration domain and w is the strain energy density

$$w = \int_0^{\varepsilon_{ij}} \sigma_{ij} d\varepsilon_{ij} \quad (7)$$

and $\sigma_{ij} n_j$ are components of the traction vector on the surface Γ, u_i are displacements, ds is the length increment along the integration domain.

Subsequently, the *J*-integral can be converted into a stress intensity factor, K_I, by using the plane strain conversion:

$$K_I = \sqrt{\frac{EJ}{1-\nu^2}} \quad .(8)$$

where E is Young's modulus and ν is Poisson ratio.

The WARP3D (Gellerud et al, 2007 and 2009) finite element solver was used to compute the *J*-integral by using a domain integration procedure. This approach is based on the methodology proposed by Li *et al.* (1985), Moran and Shih (1987) and Shih *et al.* (1986):

$$J(s) = \lim_{\Gamma \to 0} \int_{\Gamma} \left[(W + T_E) n_1 - P_{ji} \frac{\partial u_i}{\partial X_1} n_j \right] d\Gamma \quad (9)$$

where W and T_E are stress-work density and kinetic energy density per unit volume at t=0, respectively. Γ is a vanishingly small contour which lies in the principal normal plane at s, and, n is a unit vector normal to Γ. P_{ij} denotes the non-symmetric 1st Piola-Kirchhoff stress tensor which is a work conjugate to the displacement gradient expressed at the t=0 configuration as $\partial u_i / \partial X_j$ and the stress-work rate is $P_{ij} \partial u_i / \partial X_j$ per unit volume at t=0.

By using the weight functions, the contour integral is converted into an area integral for the two dimensional problem, and into a volume integral for the three dimensional problem (see Li *et al.*,(1985) and Nikishkov and Atluri (1987)):

$$\overline{J}_{a-c} = \int_{s_a}^{s_c} [J(s) q_t(s)] ds = \overline{J_1} + \overline{J_2} + \overline{J_3} \quad (10)$$

where $q_t(s)$ represents the resultant value of the weight function at the point s at the crack front and s denotes the position along the crack front segment (Al-Ani and Hancock (1991)). In Equation (10) each J-integral is defined as

$$\overline{J_1} = \int_{V_0} \left(P_{ij} \frac{\partial u_i}{\partial X_k} \frac{\partial q_k}{\partial X_j} - W \frac{\partial q_k}{\partial X_k} \right) dV_0 \quad (11)$$

$$\overline{J_2} = -\int_{V_0} \left(\frac{\partial W}{\partial X_k} - P_{ij} \frac{\partial^2 u_i}{\partial X_j \partial X_k} \right) q_k \, dV_0 \quad (12)$$

$$\overline{J_3} = -\int_{V_0} \left(T \frac{\partial q_k}{\partial X_k} - \rho \frac{\partial^2 u_i}{\partial t^2} \frac{\partial u_i}{\partial X_k} q_k + \rho \frac{\partial u_i}{\partial t} \frac{\partial^2 u_i}{\partial t \partial X_k} q_k \right) dV_0 \quad (13)$$

where q_k denotes a component of the vector weight function in the k coordinate system.

2.3 I-INTEGRAL

The interaction-integral method uses actual displacement, stress and strain fields of an equilibrium state for the boundary-value problem. A linear combination of actual fields with auxiliary fields described by Williams' solution (1957) constitutes a third superimposed equilibrium state. The computation of J for this superimposed state leads to a conservation integral composed of interacting actual and auxiliary terms that permits direct calculation of stress intensity factors (Yau et al., 1980).

The interaction integral method uses stresses, strains and displacements generated during the solution of the boundary-value problem. After superimposing actual fields with auxiliary fields corresponding to a second, arbitrary equilibrium state, fields for the superimposed state are obtained:

$$\begin{aligned}\overline{J}^{(S)}(s) &= \int_V \left[\left(\sigma_{ij}^{(1)}+\sigma_{ij}^{(2)}\right)\left(u_{j,1}^{(2)}+u_{j,1}^{(2)}\right)-W^{(S)}\delta_{1i}\right]q_{,i}\,dV + \\ &+ \int_V \left[\left(\sigma_{ij}^{(1)}+\sigma_{ij}^{(2)}\right)\left(u_{j,1}^{(1)}+u_{j,1}^{(2)}\right)-W^{(S)}\delta_{1i}\right]_{,i} q\,dV \\ &- \int_{A_3+A_4}\left(t_j^{(1)}+t_j^{(2)}\right)\left(u_{j,1}^{(1)}+u_{j,1}^{(2)}\right)q\,dA_0\end{aligned} \quad (14)$$

Here, superscripts (1) and (2) indicate actual and auxiliary fields, respectively, and (*S*) denotes the superimposed state.

The strain energy density, *W*, is function of position $x=(x_1,x_2,x_3)$, and a function of strain components ε_{ij}. For a linear-elastic, non-homogeneous material, $W^{(S)}$ is:

$$\begin{aligned}W^{(S)}(x) &= \frac{1}{2}\left(\sigma_{ij}^{(1)}+\sigma_{ij}^{(2)}\right)\left(\varepsilon_{ij}^{(1)}+\varepsilon_{ij}^{(2)}\right) \\ &= \frac{1}{2}\sigma_{ij}^{(1)}\varepsilon_{ij}^{(1)}+\frac{1}{2}\sigma_{ij}^{(2)}\varepsilon_{ij}^{(2)}+\frac{1}{2}\left(\sigma_{ij}^{(1)}\varepsilon_{ij}^{(2)}+\sigma_{ij}^{(2)}\varepsilon_{ij}^{(1)}\right) \\ &= W^{(1)}+W^{(2)}+W^{(I)}\end{aligned} \quad (15)$$

where $W^{(I)}$ is

$$W^{(I)} = \frac{1}{2}\left(\sigma_{ij}^{(1)}\varepsilon_{ij}^{(2)}+\sigma_{ij}^{(2)}\varepsilon_{ij}^{(1)}\right) \quad (16)$$

Equation 15 allows separation of Equation 14 into three parts:

$$\overline{J}^{(S)}(s) = \overline{J}^{(1)}(s)+\overline{J}^{(2)}(s)+\overline{I}(s) \quad (17)$$

where $\overline{J}^{(S)}(s)$ is the domain integral for the superimposed state, $\overline{J}^{(1)}(s)$ is the domain integral for the actual state, $\overline{J}^{(2)}(s)$ is the domain integral for the auxiliary state, and $\overline{I}(s)$ is the domain form of the interaction integral:

$$\begin{aligned}\overline{I}(s) = &\int_{V_0}\left[\sigma_{ij}^{(1)}u_{j,1}^{(2)} + \sigma_{ij}^{(2)}u_{j,1}^{(1)} - \frac{1}{2}\left(\sigma_{jk}^{(1)}\varepsilon_{jk}^{(2)} + \sigma_{jk}^{(2)}\varepsilon_{jk}^{(1)}\right)\delta_{1i}\right]q_{,i}dV_0 \\ &+ \int_{V_0}\left[\sigma_{ij}^{(1)}u_{j,1}^{(2)} + \sigma_{ij}^{(2)}u_{j,1}^{(1)} - \frac{1}{2}\left(\sigma_{jk}^{(1)}\varepsilon_{jk}^{(2)} + \sigma_{jk}^{(2)}\varepsilon_{jk}^{(1)}\right)\delta_{1i}\right]_{,i}qdV_0 \qquad (18) \\ &- \int_{A_3+A_4}\left(t_j^{(1)}u_{j,1}^{(2)} + t_j^{(2)}u_{j,1}^{(1)}\right)qdA_0\end{aligned}$$

For quasi-static, isothermal loading of homogeneous specimens in the absence of body forces and crack-face tractions, the second and third integrals of Equation 18 vanish. Since auxiliary fields correspond to an arbitrary equilibrium state, Equation 18 can be simplified with an assumption that the auxiliary state includes no crack-face tractions. The surface integral in Equation 18 thus becomes:

$$\int_{A_3+A_4} t_j^{(1)}u_{j,1}^{(2)}qdA_0 \quad (19)$$

Auxiliary fields must satisfy equilibrium, compatibility, and constitutive relations at crack-front location *s* where the asymptotic functions maintain validity for both homogeneous and graded materials (Eischen, 1987). The interaction integral is used to compute a point-wise value of:

$$I(s=b) \approx \frac{\int_{S_a}^{S_c} I(s)q_t(s)ds}{\int_{S_a}^{S_c} q_t(s)ds} = \frac{\overline{I}(s)}{A_q} \quad (20)$$

The energy release rate, *J*, for a smoothly-graded solid under mixed-mode loading and the stress intensity factors are related through:

$$J(s) = \frac{K_I^2 + K_{II}^2}{E^*(s)} + \frac{1+\nu(s)}{E(s)}K_{III}^2 \quad (21)$$

where the stress intensity factors correspond to the crack-front location, *s*. For plane-stress conditions, $E^*(s) = E$, whereas for plane-strain conditions $E^*(s) = E/(1-\nu^2)$. For the superimposed equilibrium state, the energy release rate is:

$$J^{(S)}(s) = \frac{1}{E^*(s)}\left[\left(K_I^{(1)} + K_I^{(2)}\right)^2 + \left(K_{II}^{(1)} + K_{II}^{(2)}\right)^2\right] + \frac{1+\nu(s)}{E(s)}\left(K_{III}^{(1)} + K_{III}^{(2)}\right)^2 \quad (22)$$
$$= J^{(1)}(s) + J^{(2)}(s) + I(s)$$

where

$$I(s) = \frac{1}{E^*(s)}\left(2K_I^{(1)}K_I^{(2)} + 2K_{II}^{(1)} + K_{II}^{(2)}\right) + \frac{1+\nu(s)}{E(s)}\left(2K_{III}^{(1)}K_{III}^{(2)}\right) \quad (23)$$

Equations 18, 20 and 23 define a relationship between the interaction integral and stress intensity factors. To solve for $K_I^{(1)}$, the value of *I*(s) is generated by Equation 18 where $K_I^{(2)} = 1$, $K_{II}^{(2)} = K_{III}^{(2)} = 0$, and, Equation 23 then reduces to:

$$K_I^{(1)} = \frac{E^*(s)}{2} I(s) \quad (24)$$

This procedure yields point-wise stress intensity factors along a 3-D crack front. Calculation of $K_{II}^{(1)}$ and $K_{III}^{(1)}$ follows by evaluating Equations 18, 20 and 23 with auxiliary stress intensity factors set to $K_{II}^{(2)} = 1$, $K_I^{(2)} = K_{III}^{(2)} = 0$ and $K_{III}^{(2)} = 1$, $K_I^{(2)} = K_{II}^{(2)} = 0$ respectively. For these two cases, Equation 23 yields:

$$K_{II}^{(1)} = \frac{E^*(s)}{2} I(s) \quad (25)$$

and

$$K_{III}^{(1)} = \frac{E(s)}{2(1+\nu(s))} I(s) \quad (26)$$

More information on interaction integrals and details about numerical computation of stress intensity factors are given by Gellerud et al., (2007 and 2009).

In this report, the stress intensity factors were computed using the *J*-integral and plane strain conversion for the majority of analyses performed except the investigations on complex deformation of the crack front. In these analyses, stress intensity factors for mode I, II and III of crack loading were computed using the *I*-integral.

3. EFFECT OF ENDCAP-ENDPLATE WELD DISCONTINUITY MORPHOLOGY ON STRESS INTENSITY FACTOR

3.1 DEPENDENCE OF STRESS INTENSITY FACTORS ON ENDCAP-ENDPLATE WELD DISCONTINUITY SHAPE

The endplate-to-endcap weld discontinuity is effectively a crack that shows variation in shape. Figure 3 illustrates the actual endplate-to-endcap weld discontinuity from results of testing. In this analysis, the endcap has a round shape. The shape of the endcap-endplate weld discontinuity was modeled to be round or elliptical. Numerical simulations were performed to determine how these characterizations affect the computed stress intensity factors. The representative depth of the discontinuity and various circumferential extensions were applied. The reference case was a fully circumferential crack with round shape.

3.2 DEVELOPED FINITE ELEMENT MODELS

Finite element models were developed using 20 node hexahedral elements with reduced integration order. Special mesh refinement was applied at the crack front as illustrated in Figures 4, 5 and 6. The spider mesh type was used. Twenty rings and eight elements segments around a crack were used to obtain high quality solutions. There were two symmetry planes applied in these models. The first symmetry plane was in the vertical plane (XY), and the second symmetry plane was in the crack plane (YZ) as presented Figure 7. This approach was chosen in order to reduce model size and computational time. The load was applied by bending stress at the free end of the rod.

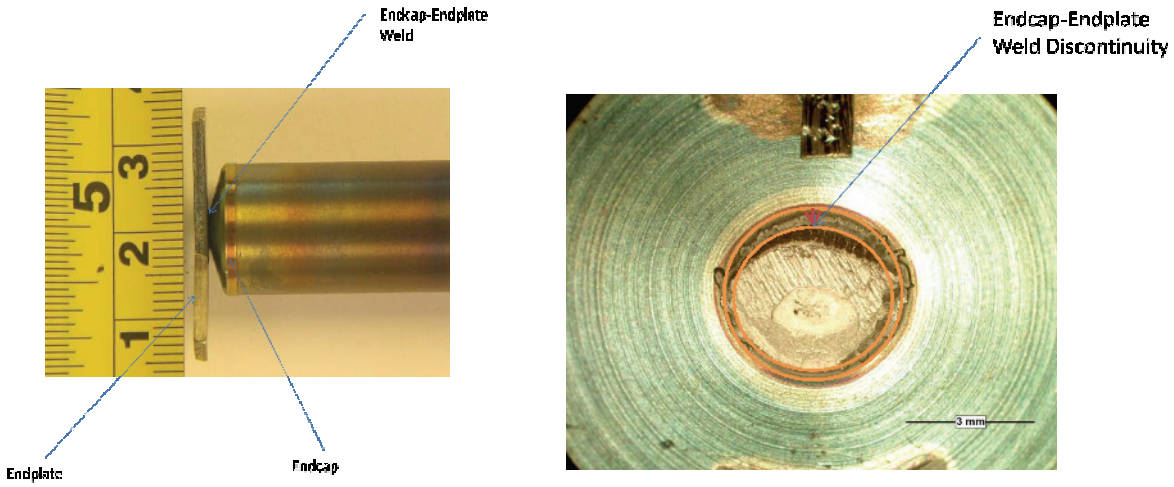

Figure 3: Endplate-to-Endcap Discontinuity

The finite element models were developed using MSC Patran software (MSC Software Corporation, 2005) and PCL script language. The WARP3D (Gellerud et al., 2007 and 2009) finite element solver was used. This computer code is specialized for fracture mechanics problems. The crack driving force in terms of *J*-integral was calculated.

The computed *J*-integral was converted to stress intensity factor *K* by applying plane strain conversion:

$$K_I = \sqrt{\frac{E\,J}{1-\nu^2}} \quad (1)$$

where *E* was Young's modulus and *v* was Poisson's ratio.

The surface cracks with round or elliptical shape were modeled. The elliptical shape of the crack was described as the surface elliptical crack after transformation from plate to rod. Typically, the major and minor axes were the crack length and the crack depth respectively. However, when the crack length is short the major and minor axes could be reversed. The modeling was challenging due to complexity of mesh generation at the crack front; however, high quality meshes were obtained.

Numerical simulations were performed using material properties given in Table 1. Linear elastic material response was assumed.

Table 1: Mechanical Properties of Endcap-Endplate Material

Young's Modulus	Poisson's Ratio
94,500 MPa	0.4

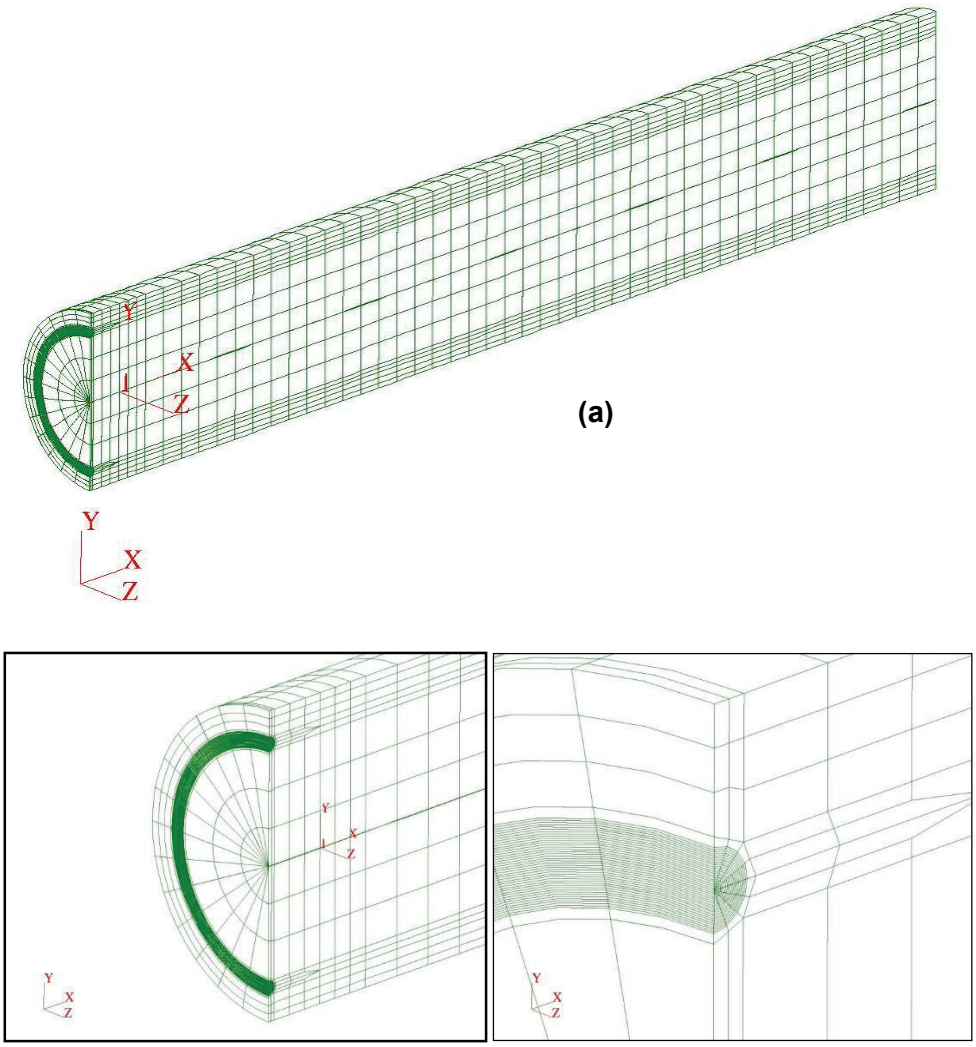

Figure 4: Reference Case: Finite Element Model of a Rod with a Fully Circumferential Surface Crack (a) Half Symmetry Model, (b) Details of Mesh Refinement at the Crack

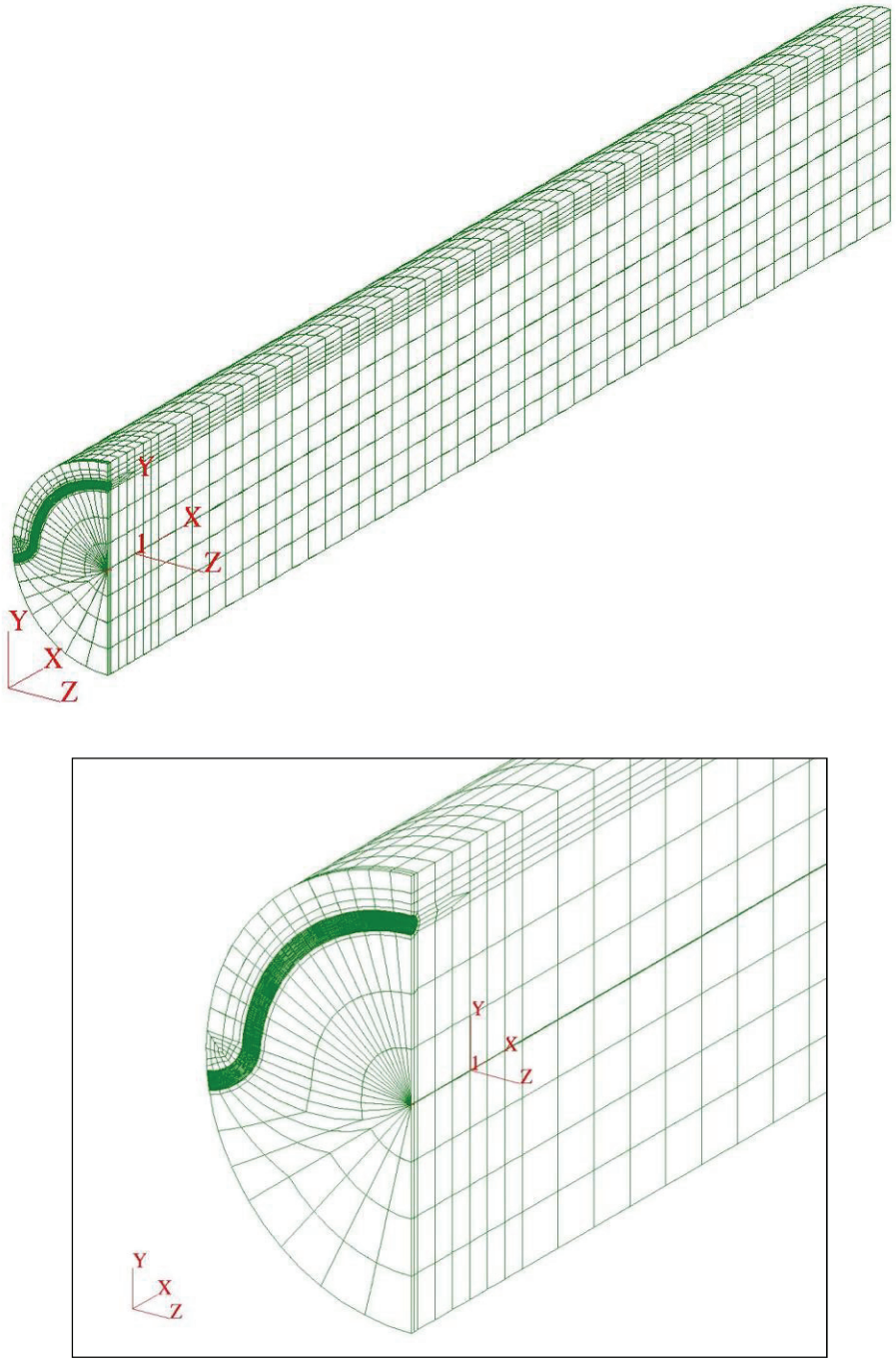

Figure 5: Finite Element Model of a Rod with a Round Circumferential Surface Crack with Limited Extension

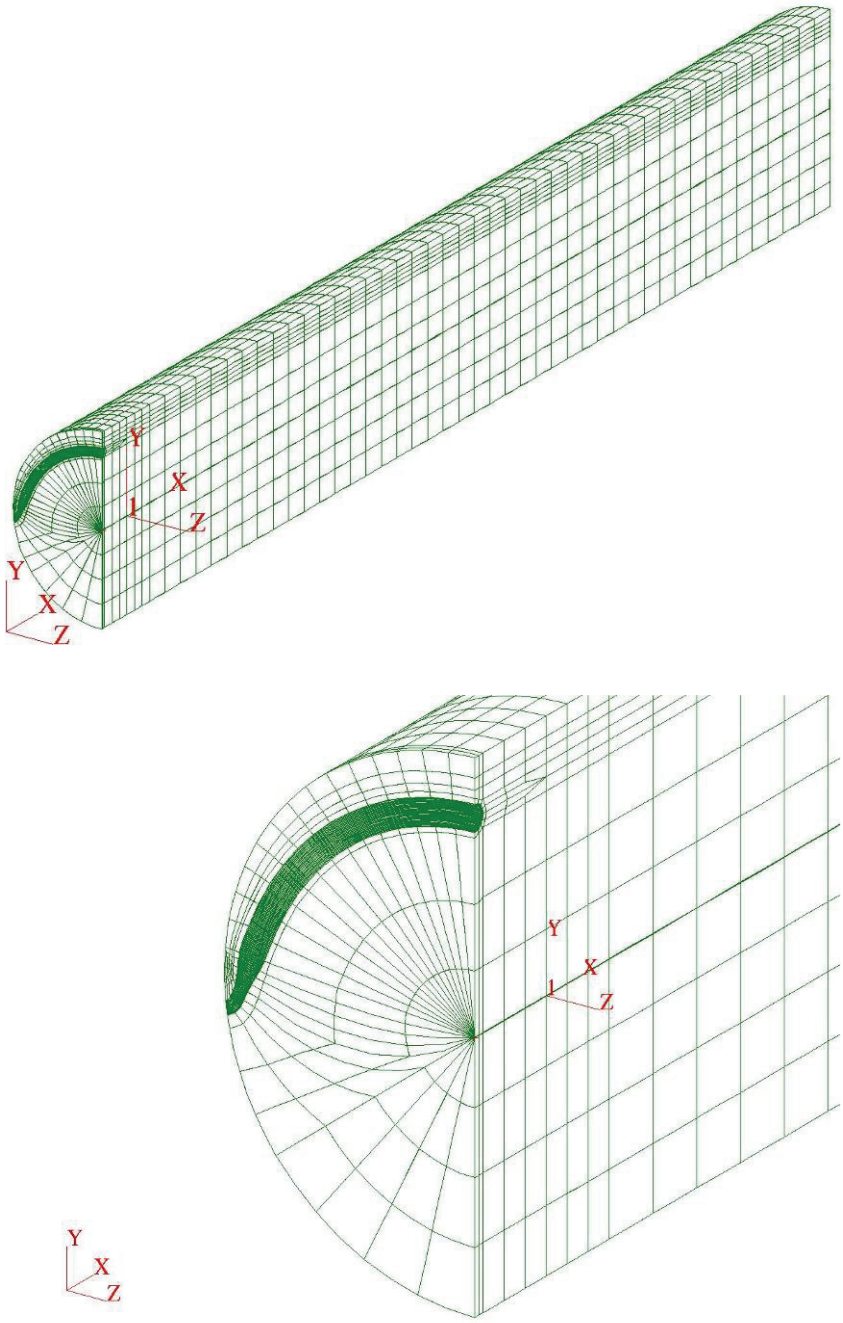

Figure 6: Finite Element Model of a Rod with an Elliptical Circumferential Surface Crack with Limited Extension

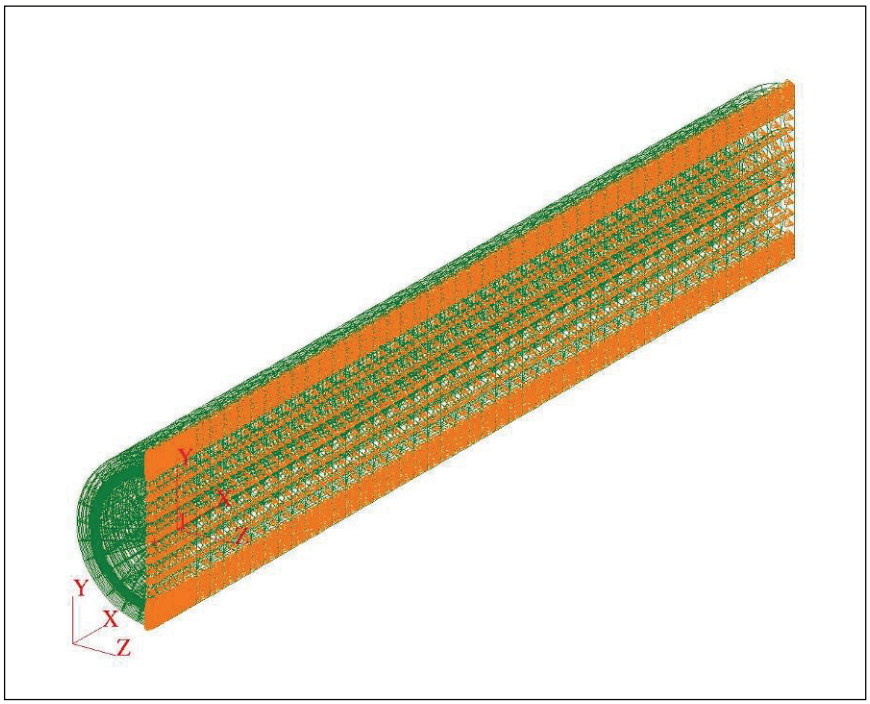

(a)

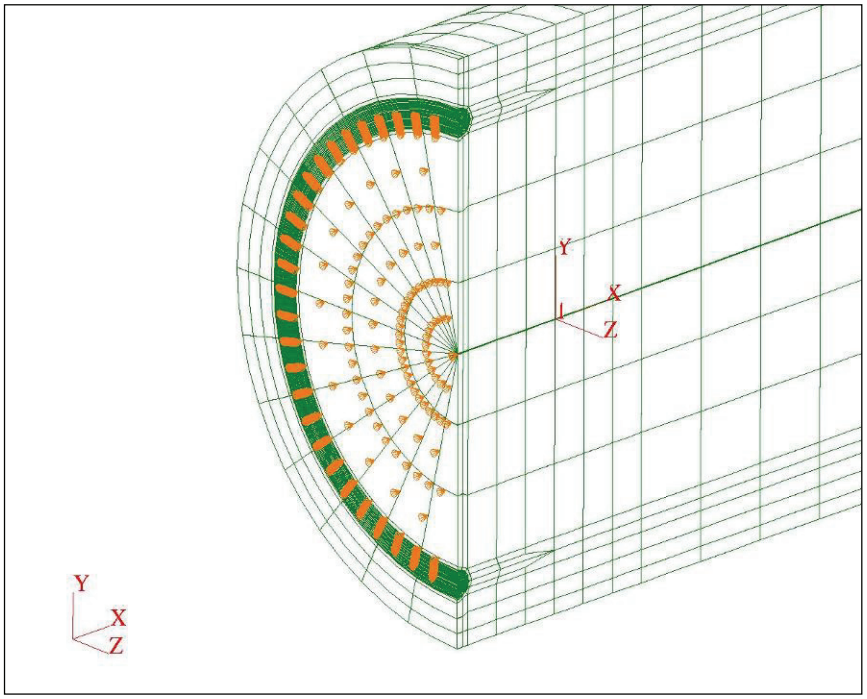

(b)

Figure 7: Boundary Conditions Applied to the Finite Element Model of a Rod with a Fully Circumferential Surface Crack (a) Symmetry Plane XY, (b) Symmetry Plane YZ

3.3 STRESS INTENSITY FACTORS AT THE ENDCAP-ENDPLATE WELD DISCONTINUITY

Numerical simulations were performed for three cases: a fully circumferential surface crack with constant depth (reference case), a limited extension round surface crack with constant depth and a limited extension surface elliptical crack. In this analysis, the crack depth was chosen as 0.51 mm and is representative of weld discontinuity depths found in the DHC experimental program (Shek and Wasiluk, 2009). The stress intensity factors were computed at the location of the maximum crack driving force for a particular crack extension. These cracks have limited crack extension angle. However, the location of the maximum stress intensity factor could change depending on surface crack dimensions. Table 2 presents the computed stress intensity factors for constant depth round and elliptical surface cracks with limited extension. A zero degree angle was assigned to a crack tip location in the vertical plane. Constant depth round surface cracks showed slightly higher stress intensity factors over elliptical cracks. This means that the shape of the weld discontinuity introduces some uncertainty to the calculated stress intensity factor; however, it is small. However, this needs to be confirmed for the actual fuel element geometry.

The effect of limited and fully circumferential crack extension is illustrated in Figure 8. Computed stress intensity factors for constant depth and elliptical cracks were normalized by the stress intensity factor of 9.7 MPa$\sqrt{\text{m}}$ computed for a fully circumferential crack. The effect of limited crack extension is strong for crack extension below 90°. This is a situation when an endplate-to-endcap weld discontinuity is limited.

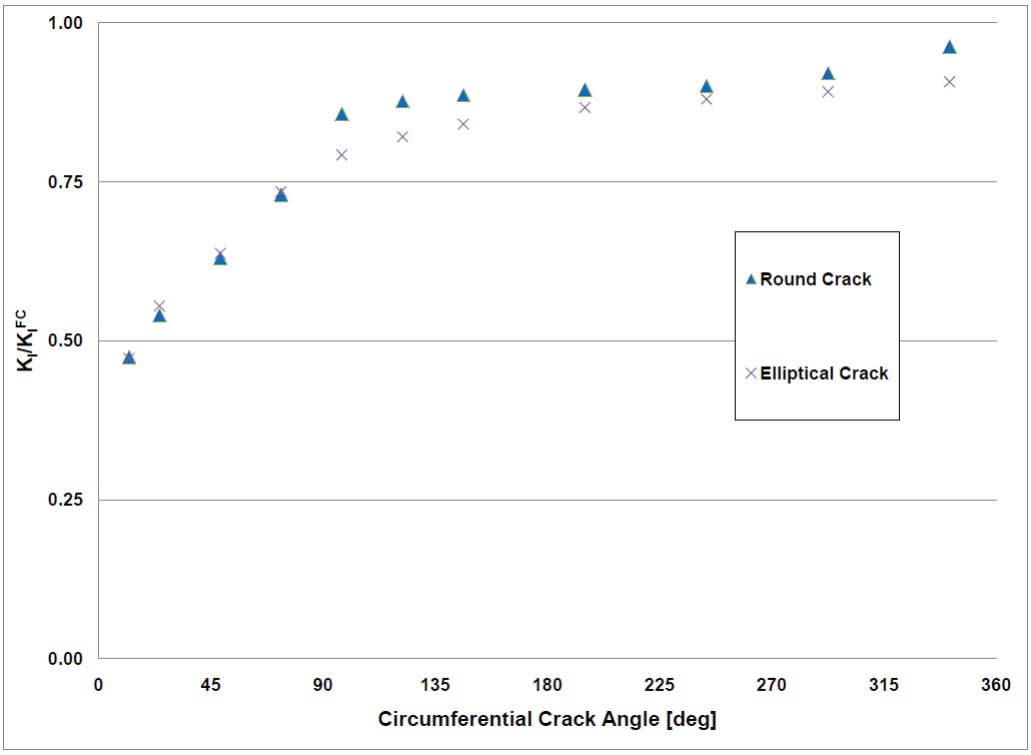

Figure 8: Effect of Surface Crack Extension on Computed Stress Intensity Factor

Table 2: Stress Intensity Factors for Surface Round and Elliptical Cracks

Case No.	Crack Length	Crack Angle	J^{EL}	K_I^{EL}	J^{CD}	K_I^{CD}	J_I^{CD}/J_I^{EL}	K_I^{CD}/K_I^{EL}
	(mm)	(deg)	N/mm	MPa√m	N/mm	MPa√m		
			Elliptical		Round			
1	0.5	12	0.19	4.6	0.19	4.6	1.01	1.00
2	1.0	24	0.26	5.4	0.24	5.2	0.95	0.97
3	2.0	49	0.34	6.2	0.33	6.1	0.98	0.99
4	3.0	73	0.45	7.1	0.44	7.1	0.99	0.99
5	4.0	98	0.52	7.7	0.61	8.3	1.17	1.08
6	5.0	122	0.56	8.0	0.64	8.5	1.14	1.07
7	6.0	146	0.59	8.1	0.66	8.6	1.11	1.05
8	8.0	195	0.63	8.4	0.67	8.7	1.07	1.03
9	10.0	244	0.65	8.5	0.68	8.7	1.05	1.02
10	12.0	293	0.66	8.6	0.71	8.9	1.07	1.03
11	14.0	341	0.69	8.8	0.77	9.3	1.13	1.06

4. STRESS INTENSITY FACTORS FOR GE FUEL ELEMENTS

The effect of geometry of the endcap-endplate weld discontinuity on the calculated stress intensity factor for GE-2 fuel elements was already discussed in Shek and Wasiluk (2009). Results from several finite element models of increasing complexity were reported. The effect of the V-notch shape was found to be negligible on the calculated stress intensity factor. Therefore, the stress concentration factor is calculated assuming a crack-like behavior. The crack depth is defined as a combination of the notch depth and the depth of the endcap-endplate weld discontinuity.

GE-1 type fuel elements are different from GE-2 type. They have different geometry and endcap-endplate weld discontinuity as can be observed from Figure 10. In the GE-1 design, the position of the endcap is moved from the centre of the endplate. This suggested a sensitivity of stress intensity factors on the characterization of the geometry and boundary conditions.

4.1 GENERAL ELECTRIC DESIGN GE-1 FUEL ELEMENTS

Three dimensional finite element models of the GE-1 type fuel element were created using 20-node hexahedral elements. Figure 11 presents details of the mesh developed. The spider type mesh was used at the crack tip similarly to the other previously developed models. A one symmetry plane was applied as shown in Figure 12. The rigid boundary conditions were applied to two external surfaces of the endplate. In this particular model, the endplate width was the same as the diameter of the endcap. The actual geometry from test 09_125 (Shek, 2010) was used in these calculations. This model is named GE-1 Model I.

Figure 13 presents the distribution of the calculated stress intensity factor around the circumference. The stress intensity factors change and the maximum value is at 45° from the vertical plane, which is the plane of the applied bending moment. This result suggests the importance of endplate deformation on the calculated crack driving force. In order to explore it further, the boundary conditions at the endplate were modified as in Figure 14 (GE-1 Model Ia). The outer surface at the top became rigid. The application of this boundary condition changed calculated stress intensity factor dramatically. The maximum value of the stress intensity factor is now at the symmetry plane, see Figure 15. Also, the maximum value of the stress intensity factor has changed. Figure 16 compares the stress intensity factors for these two different boundary conditions.

The effect of location of the endcap weld regarding the endplate was studied. The finite element model presented in Figure 17 was utilized. This model is named GE-1 Model II. The boundary conditions applied were the same as in GE-1 Model I. However, the obtained distribution of stress intensity factor is similar to the results from GE-1 Model Ia, see Figures 18 and 19. The maximum stress intensity factor from Model GE-1 II is very similar to the one obtained from GE-1 Model I.

Deformation of the endcap-endplate weld discontinuity was investigated further by calculating stress intensity factors for crack load mode I, II and III. It was found that the crack front is under complex deformation as illustrated in Figures 20 and 21 above. The effect of mode II and III loading is significant in GE-1 Model I. This complex deformation at the crack could explain the observed crack propagation in different planes.

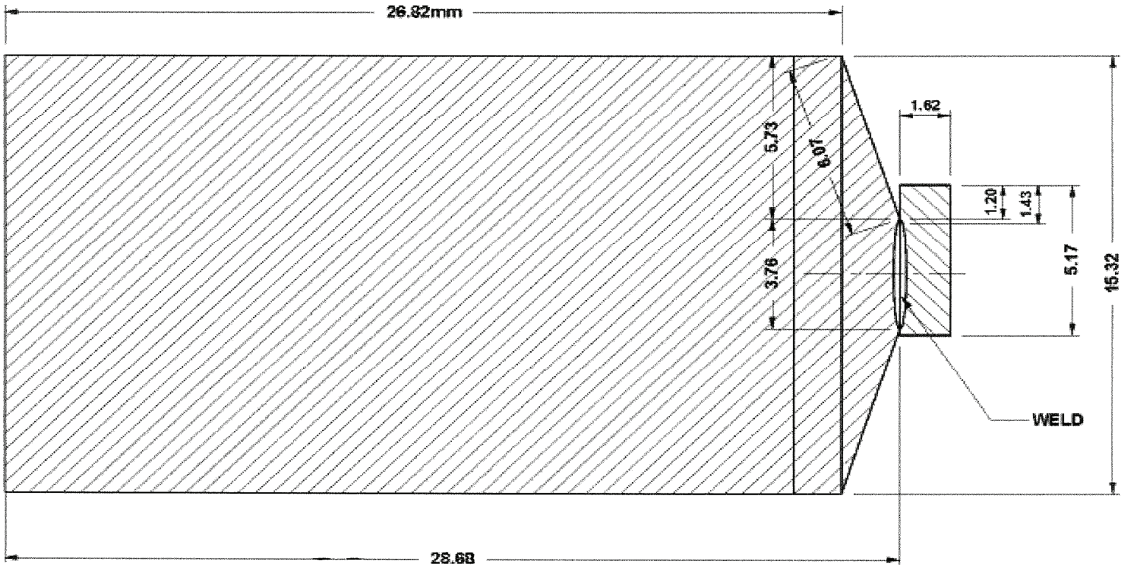

Figure 9: Geometry of Tested Fuel Element GE-1 -Test 09_125 (Shek, 2010)

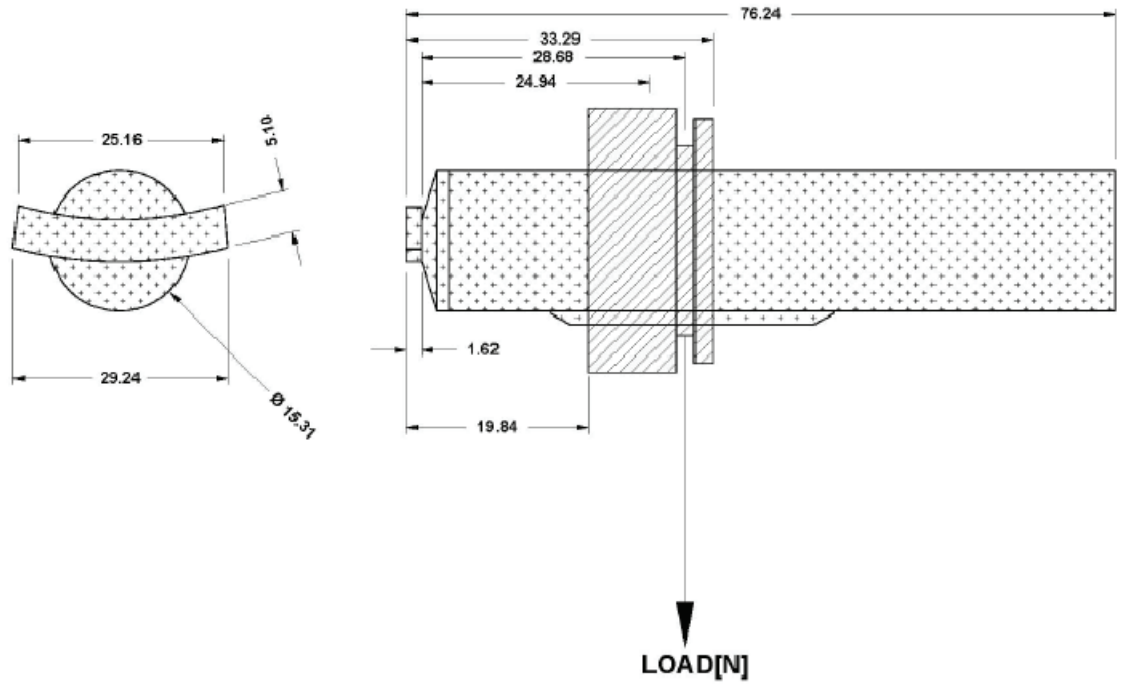

Figure 10: Load Setup for Tested Fuel Element GE-1 -Test 09_125 (Shek, 2010)

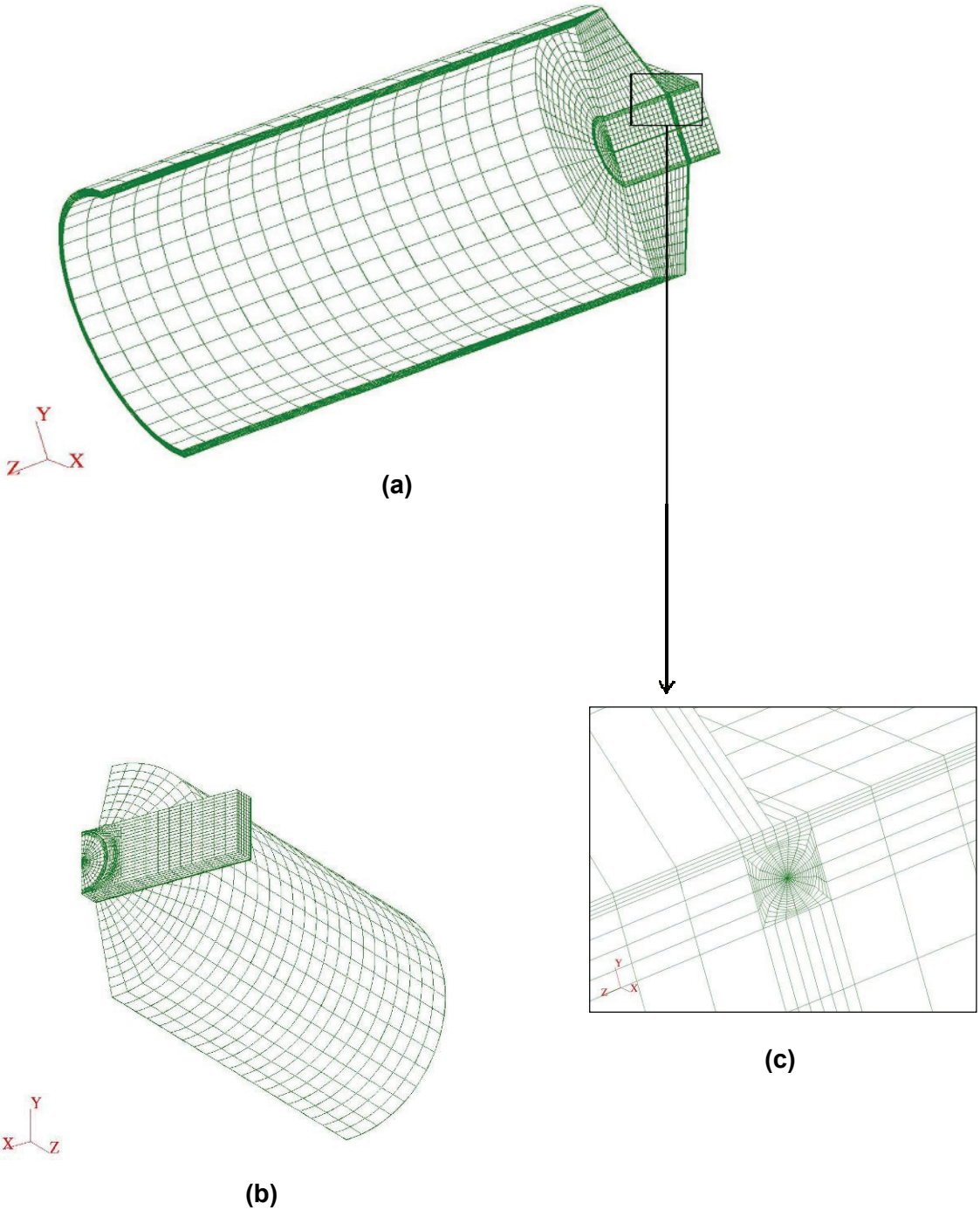

Figure 11: Finite Element Model I of GE-1 Fuel Element (a) Finite Element Model, (b) Crack Tip Mesh (Detail), (c) Top View

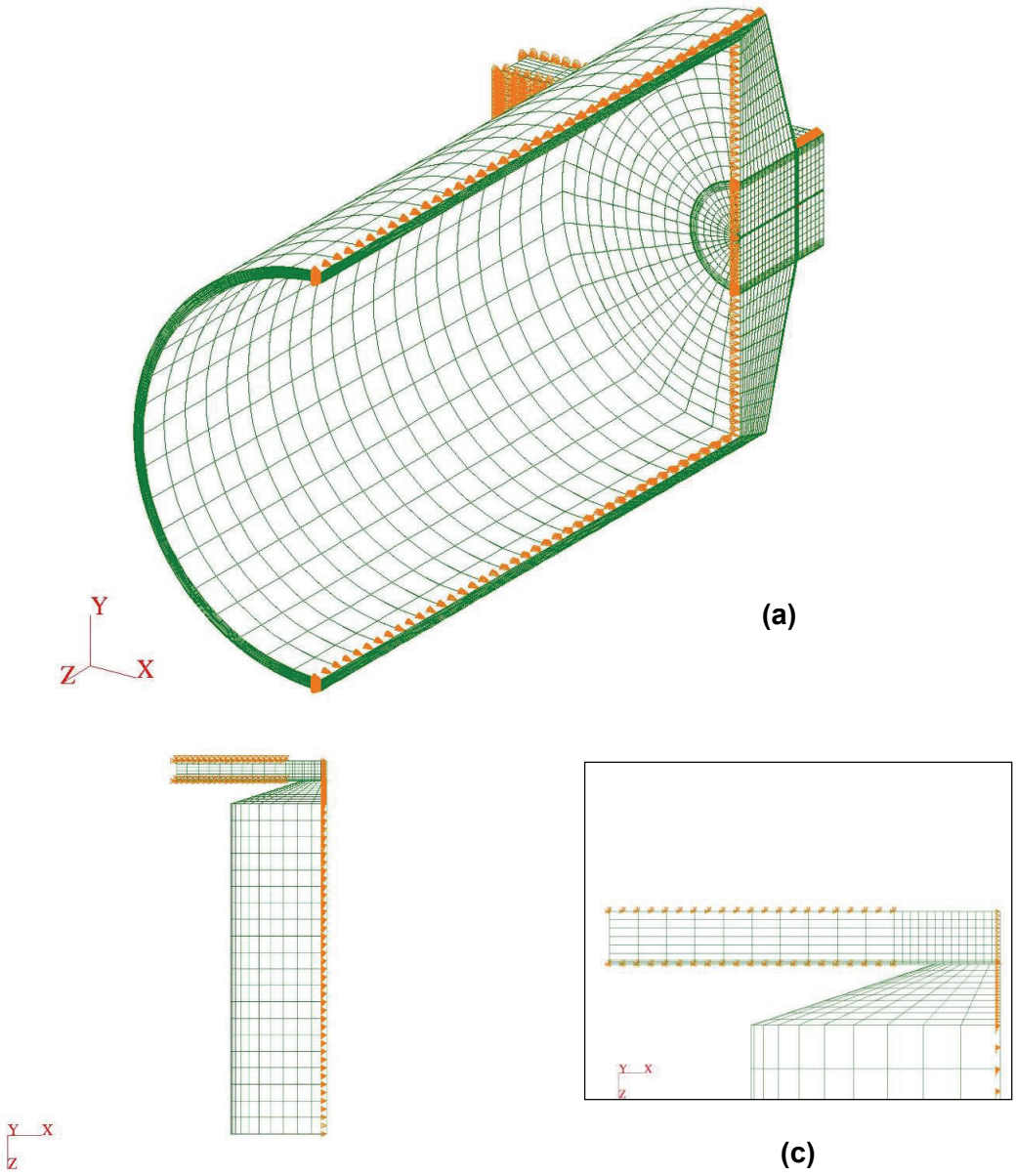

Figure 12: Boundary Conditions Applied in Finite Element Model I of the GE-1 Fuel Element, (a) Finite Element Model, (b) Top View, (c) Top View (Detail)

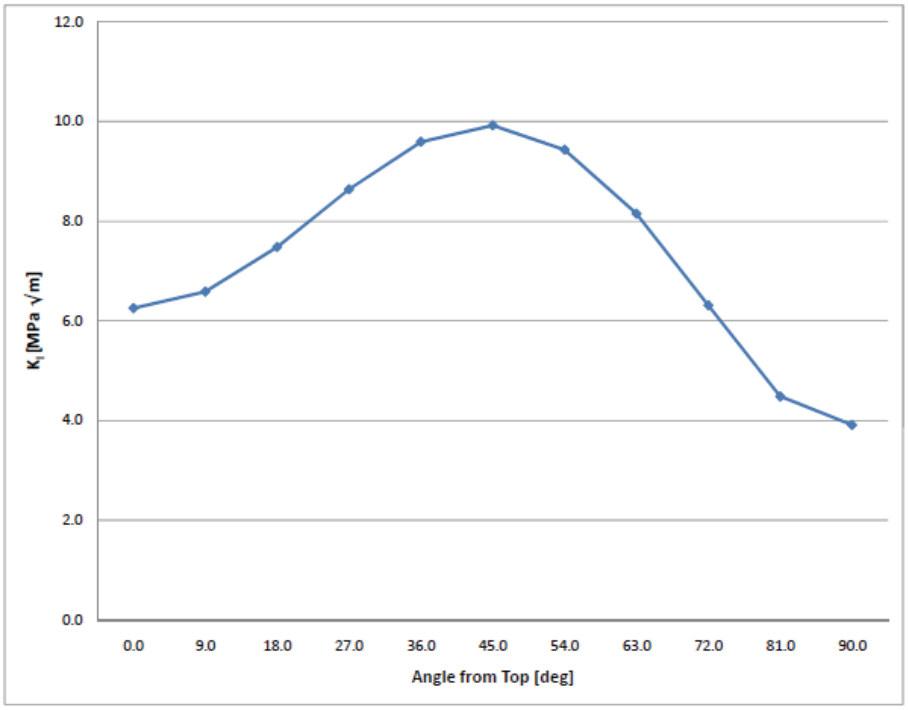

Figure 13: Distribution of Stress Intensity Factor from Finite Element Model I of GE-1 Fuel Element

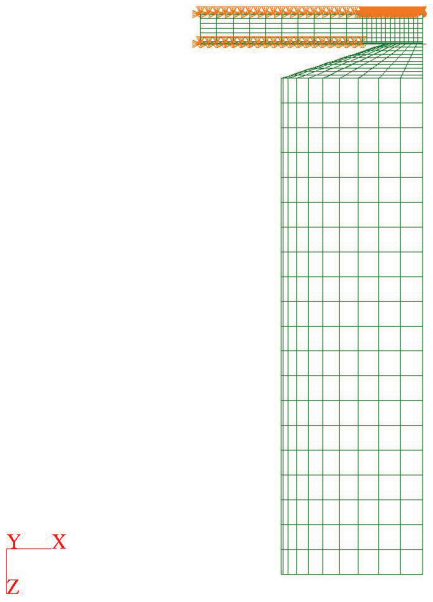

Figure 14: Fixed Top Plane Applied in Finite Element Model I (a) of GE-1 Fuel Element

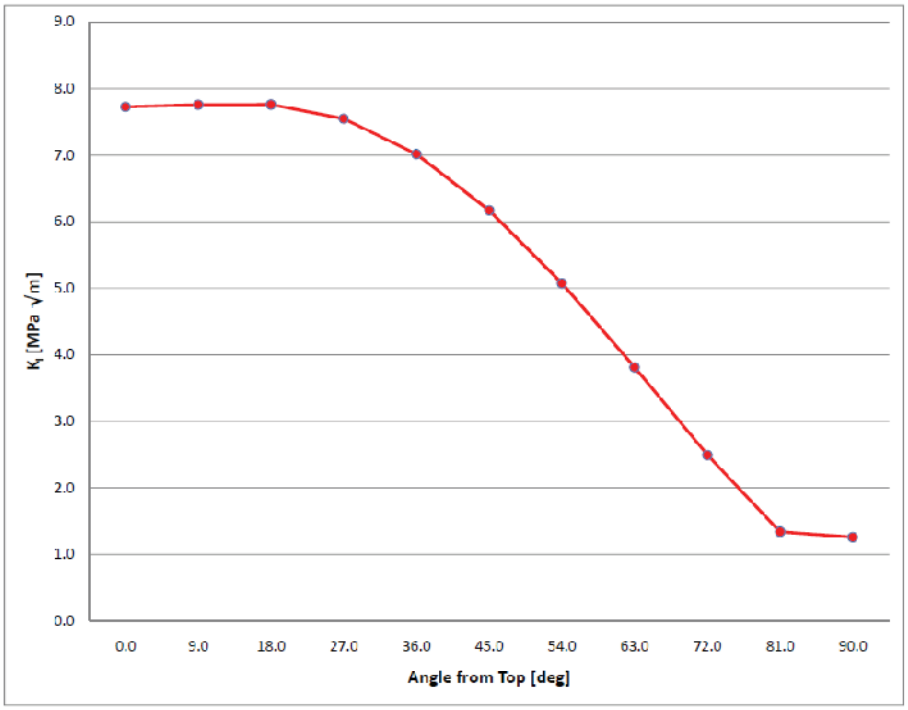

Figure 15: Distribution of Stress Intensity Factor from Finite Element Model Ia with Fixed End of GE-1 Fuel Element

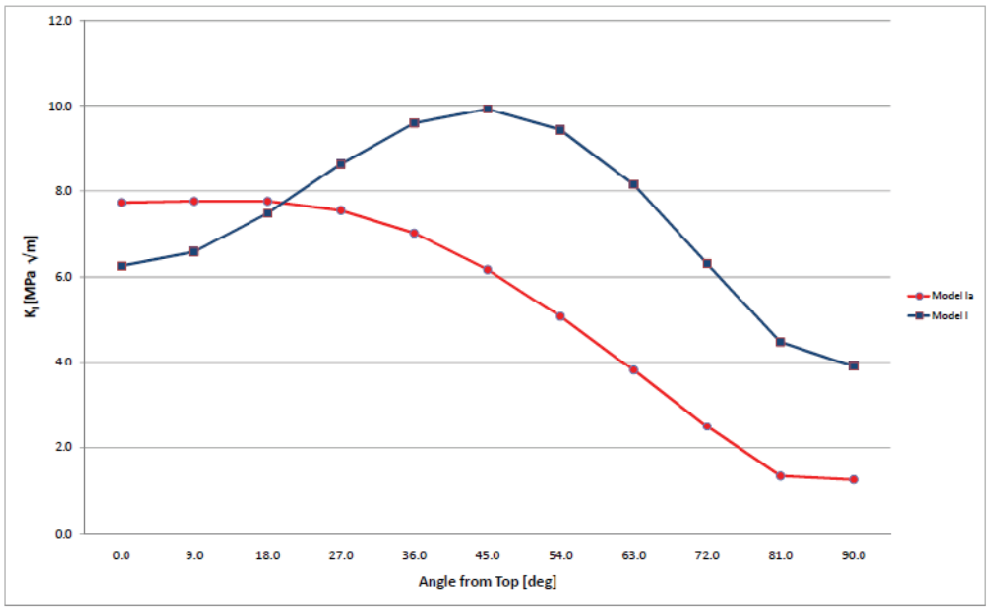

Figure 16: Comparison of Stress Intensity Factor for GE-1 Fuel Element with and without Fixed End Plane

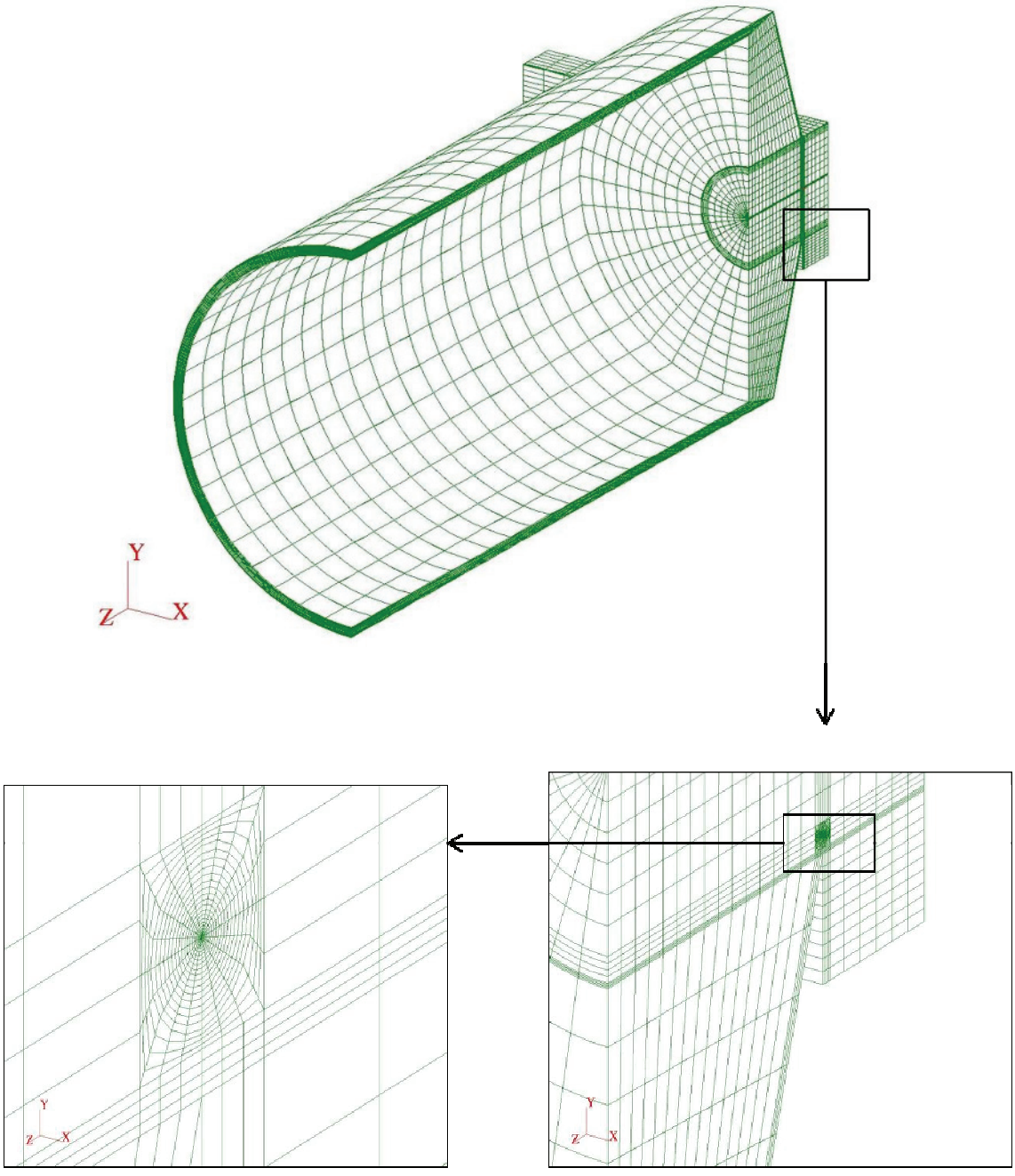

Figure 17: Finite Element Model II of GE-1 Fuel Element

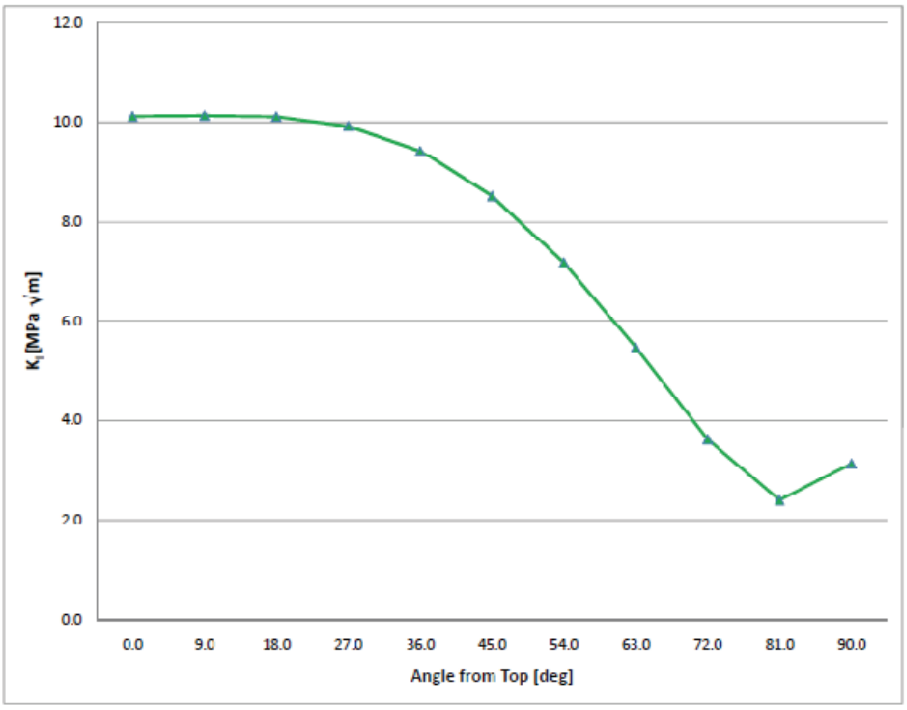

Figure 18: Distribution of Stress Intensity Factor from Finite Element Model II of GE-1 Fuel Element

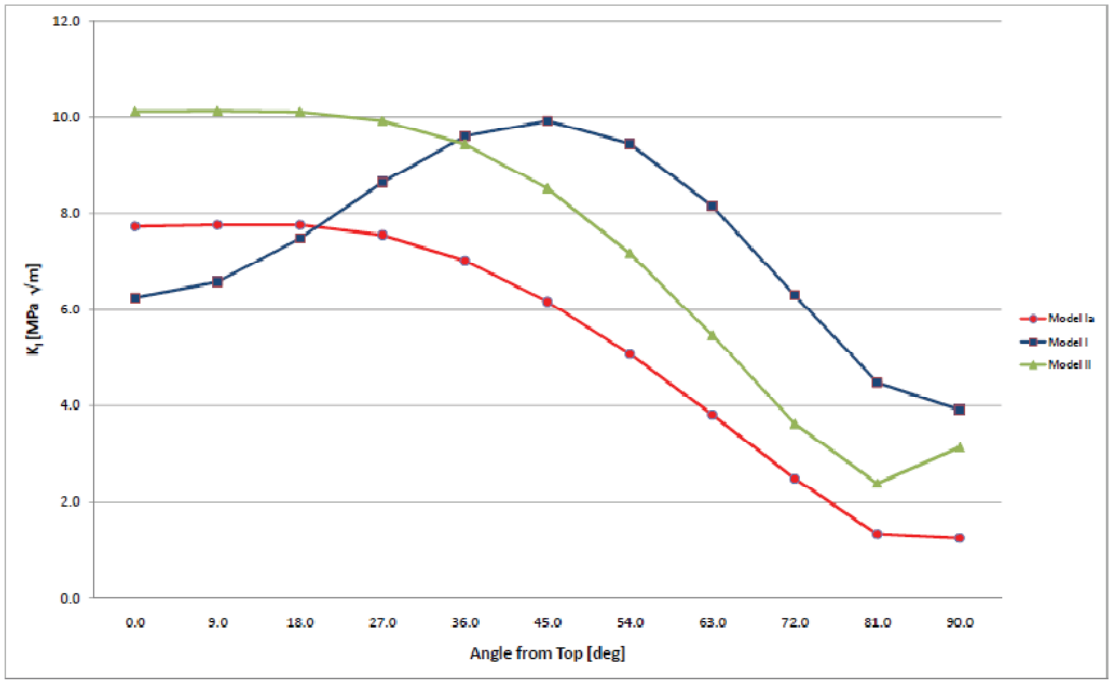

Figure 19: Stress Intensity Factors from Finite Element Model I and II GE-1 Fuel Element

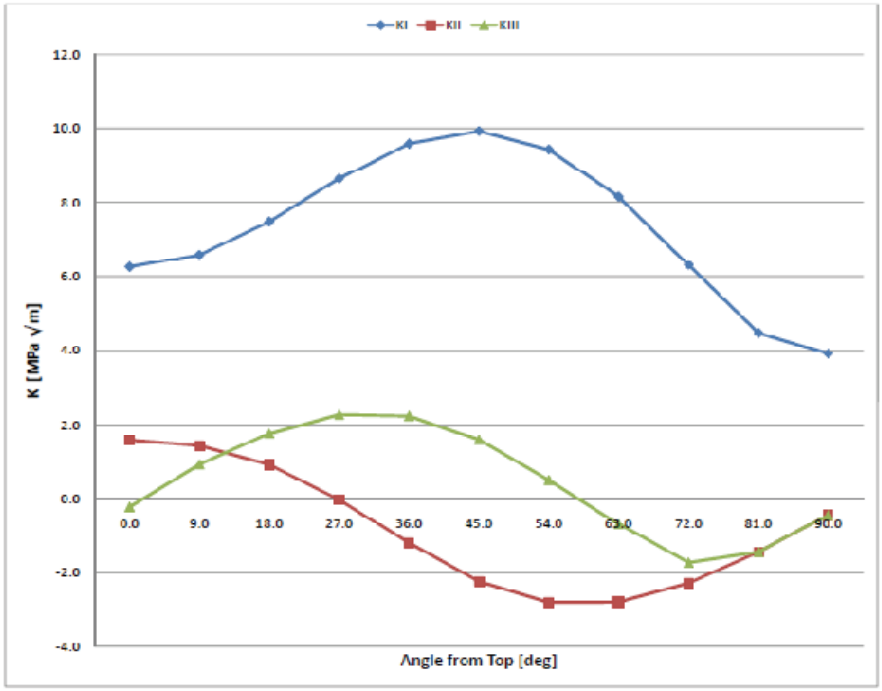

Figure 20: Stress Intensity Factors from Finite Element Model I of GE-1 Fuel Element

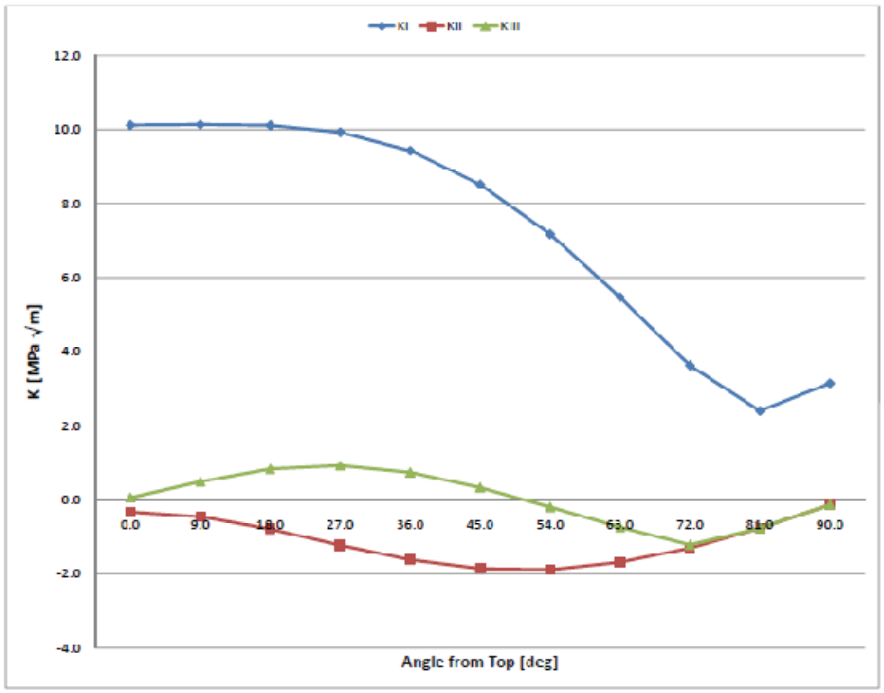

Figure 21: Stress Intensity Factors from Finite Element Model II of GE-1 Fuel Element

4.2 GENERAL ELECTRIC DESIGN GE-2 FUEL ELEMENTS

The fuel element geometry and load setup of the GE-2 fuel bundle is shown in Figures 22 and 23. The developed finite element model is presented in Figure 24. This model is named GE-2 Model I. The applied boundary conditions are similar to these in GE-1 Model I and are presented in Figure 25. Numerical calculations were performed for the geometry of the fuel

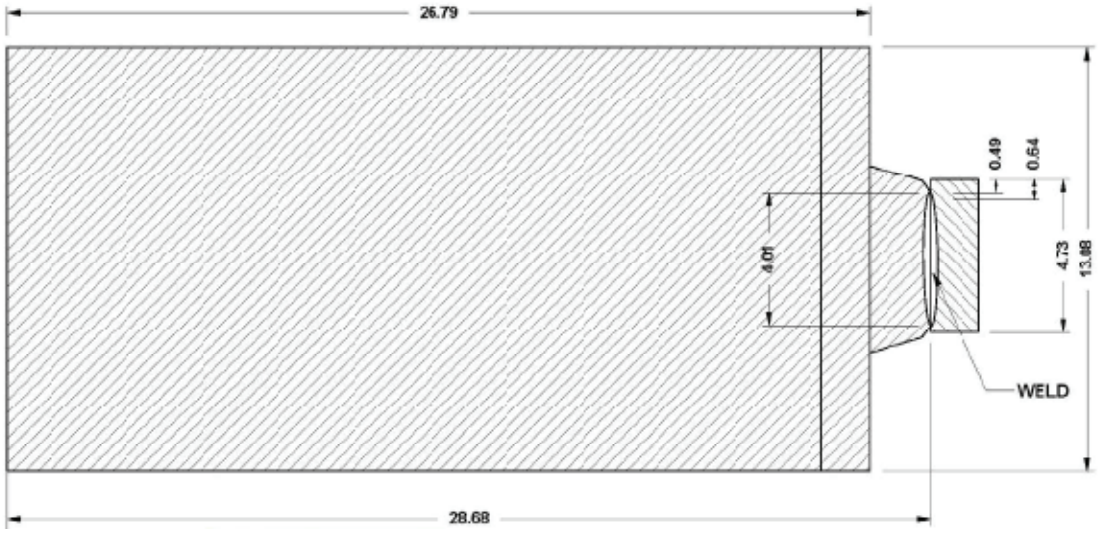

Figure 22: Geometry of Tested Fuel Element GE-2 -Test 09_120 (Shek, 2010)

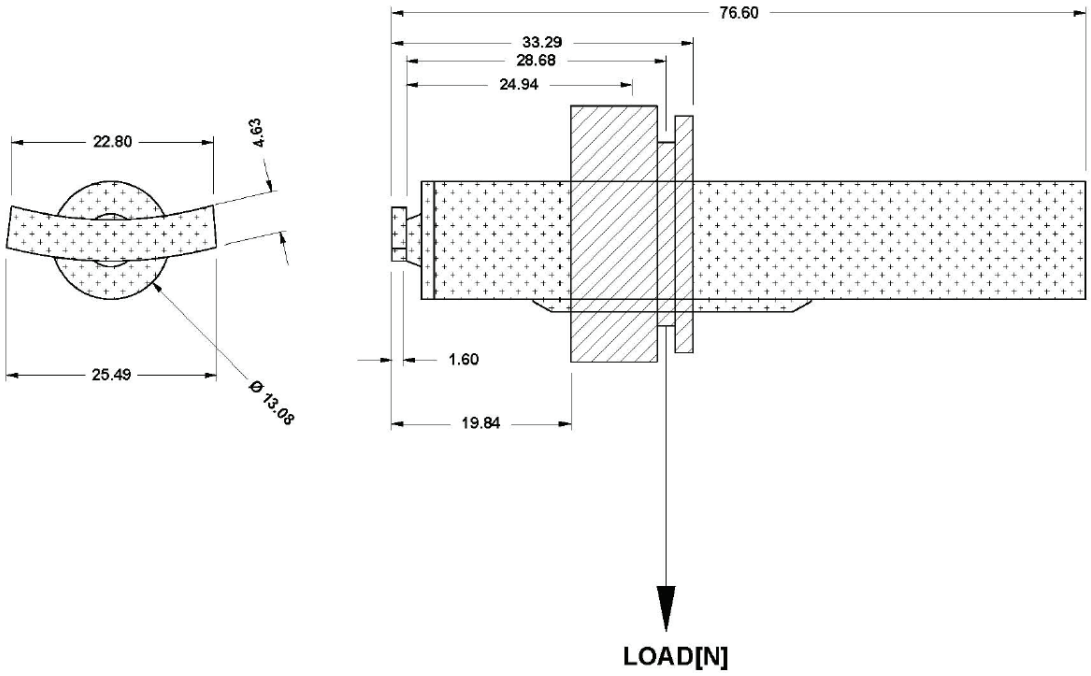

Figure 23: Load Setup for Tested Fuel Element GE-2 -Test 09_120 (Shek, 2010)

element tested in the test 09_120 Shek (2010). Figure 26 shows the distribution of the computed stress intensity factors for the load at DHC initiation during the experiment. This distribution is similar to the results from GE-1 Model I. The maximum value is observed at 45°. At this angle, the crack showed in a complex deformation state mode I, II and III as illustrated in Figure 27.

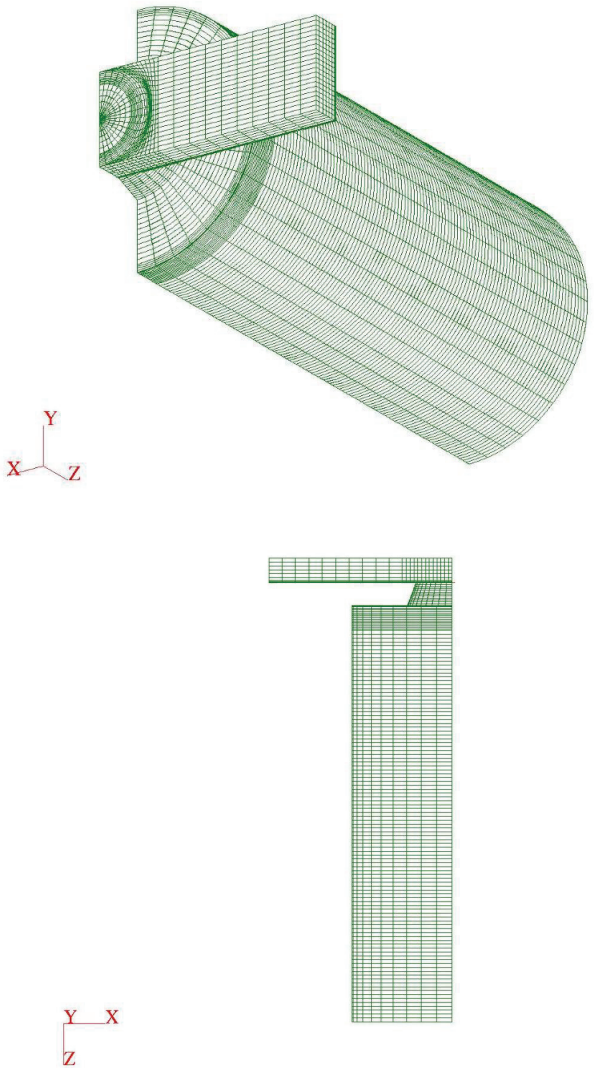

Figure 24: Finite Element Model I of GE-2 Fuel Element

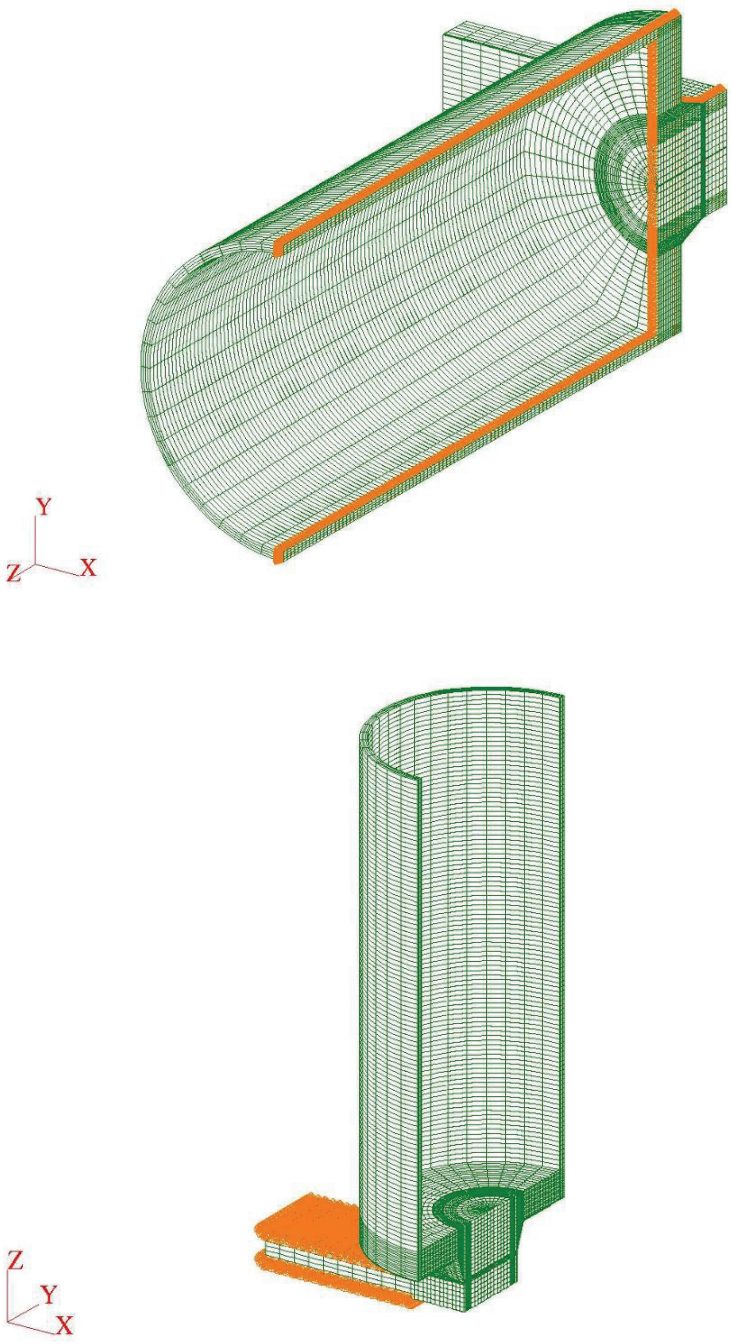

Figure 25: Boundary Conditions Applied in Finite Element Model I of GE-2 Fuel Element

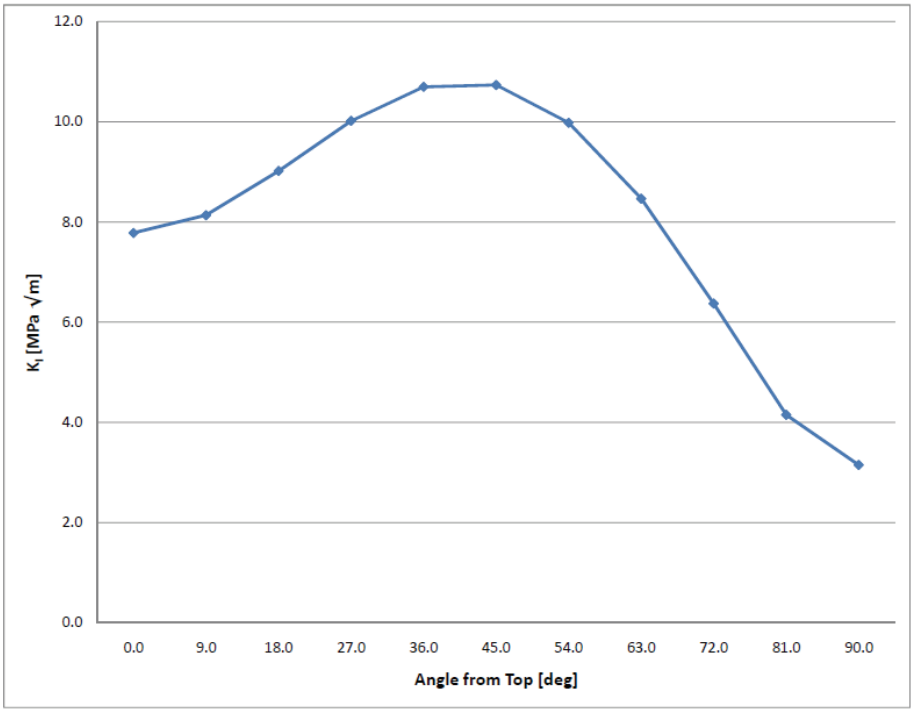

Figure 26: Stress Intensity Factor from Model I of Fuel Element GE-2

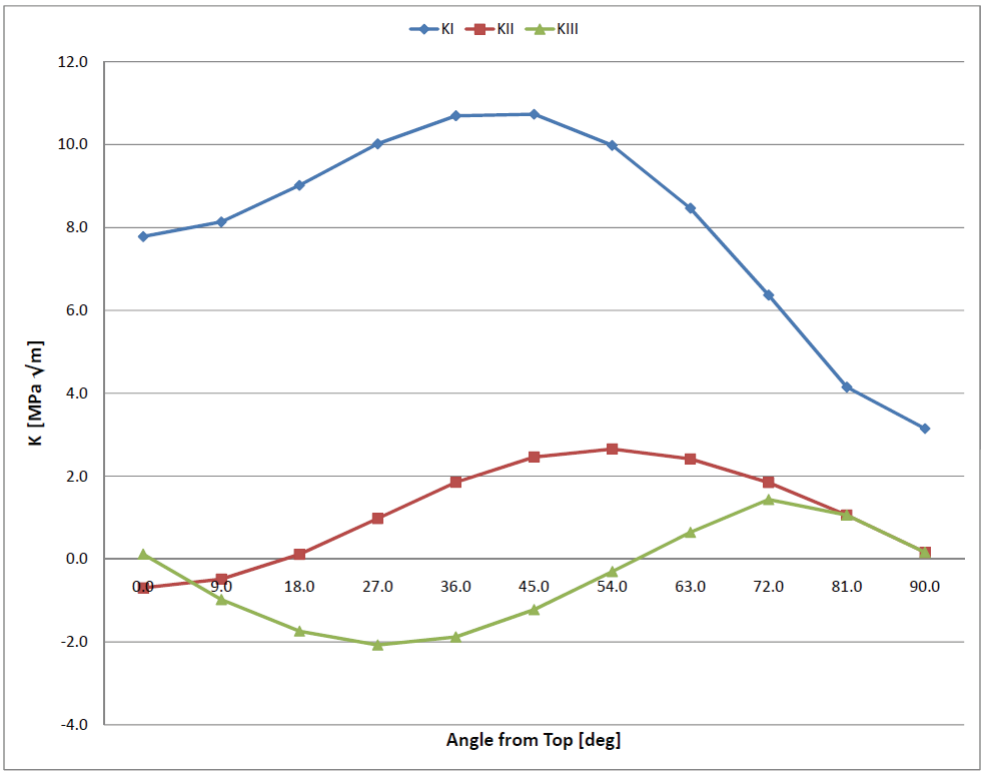

Figure 27: Profiles of Stress Intensity Factors of Fuel Element GE-2

5. CONCLUSIONS

(a) The calculated stress intensity factors show a strong dependence on circumferential extension of an endplate-to-endcap weld discontinuity up to a ninety degree from the top of the weld. Beyond the ninety degrees, the susceptibility is less pronounced.

(b) The shape of the endplate-to-endcap weld discontinuity, round versus elliptical, was found to play a minor role in the representative depth of the endplate-to-endcap weld discontinuity.

(c) Deformation of the endplate significantly changes distribution of stresses at the endplate-to-endcap weld discontinuity.

(d) The maximum value of stress intensity factor could be re-located from the vertical plane to a plane at forty five degree from the vertical for a GE-1 type fuel element.

(e) The position of the endcap relative to the endplate strongly affects the stress intensity factor. The maximum value of the stress intensity factor is shifted from the plane at forty five degrees to the vertical plane.

(f) Uncertainties in characterization of the endplate-to-endcap weld discontinuity leads to considerable error in the calculated stress intensity factor.

(g) An endplate-to-endcap weld discontinuity could be under complex combined modes I, II and III crack loading during both experiment and during fuel bundle storage.

ACKNOWLEDGEMENTS

The author would like to acknowledge Dr. J. Freire-Canosa of NWMO and Mr. T. Lampman of AMEC-NSS for providing helpful discussions and comments throughout the program.

REFERENCES

Al-Ani, A.M. and J.W. Hancock. 1991. J-Dominance of Short Cracks in Tension and Bending. J. Mech. Phys. Solids, 39, 23-43

Eischen, J.W. 1987. Fracture of Non-homogeneous Materials, Int J Fracture, 34, 3-22.

Gellerud A., K. Koppenhoefer, A. Roy, S. Roychowdhury, M. Walters, B. Bichon, K. Cochran, A. Carlyle and R.H. Dodds Jr. 2007. WARP3D-Release 15.8: 3-D Dynamic Nonlinear Fracture Analysis of Solids Using Parallel Computers and Workstations. User's Manual.

Gellerud, A., K. Koppenhoefer, A. Roy, S. Roychowdhury, M. Walters, B. Bichon, K. Cochran, A. Carlyle and R.H. Dodds Jr. 2009. WARP3D-Release 16.2: 3-D Dynamic Nonlinear Fracture Analysis of Solids Using Parallel Computers and Workstations. User's Manual.

Hutchinson, J.W. 1968. Singular Behavior at the End of a Tensile Crack in a Hardening Material. J. Mech. Phys. Solids, 16, 13-31.

Li, F.Z., C.F. Shih and A. Needleman. 1985. A Comparison of Methods for Calculating Energy Release Rates. Eng Fract Mech, 21, 405-421.

Moran, B. and C.F. Shih. 1987. A General Treatment of Crack Tip Contour Integrals. Int J Fracture, 35, 295-310.

Moran, B. and C.F. Shih. 1987. Crack Tip and Associated Domain Integrals from Momentum and Energy Balance. Eng Fract Mech, 27, 615-642.

MSC Software Corporation. 2005. MSC Patran 2005 Reference Manual.

Nikishkov, G.P. and S.N. Atluri. 1987. Calculation of Fracture Mechanics Parameters for an Arbitrary Three-dimensional Crack, by the 'Equivalent Domain Integral' Method. Int J Num Met Eng, 24, 1801-1827.

Rice, J.R. and G.F. Rosengren, 1968. Plane Strain Deformation Near a Crack Tip in a Power-law Hardening Material. J. Mech. Phys. Solids, 16, 1-12.

Shek, G.K. and B.S. Wasiluk. 2009. Development of Delayed Hydride Cracking Test Apparatus and Commissioning Tests for CANDU Fuel Bundle Assembly Welds. Nuclear Waste Management Organization. NWMO TR-2009-08. Toronto. Canada.

Shek, G.K. 2010. Determination of the Threshold Stress Intensity Factor and Velocity of Delayed Hydride Cracking of Endplate Welds in CANDU Fuel Bundles with Different Design and Manufacturers. Nuclear Waste Management Organization. NWMO TR-2010-25. Toronto. Canada.

Shih, C.F., B. Moran and T. Nakamura. 1986. Energy Release Rate Along a Three Dimensional Crack Front in a Thermally Stressed Body. Int J Fracture, 30, 79-102.

Williams, M.L. 1957. On the Stress Distribution of the Base of a Stationary Crack. Journal of Appl Mech. ASME, Vol. 24, 111-114.

Yau, J.F., S.S. Wang and H.T. Corten. 1980. A Mixed-mode Crack Analysis of Isotropic Solids Using Conservation Laws of Elasticity. ASME Journal of Applied Mechanics, 47, 335-341.